RSC Advances



This is an *Accepted Manuscript*, which has been through the Royal Society of Chemistry peer review process and has been accepted for publication.

Accepted Manuscripts are published online shortly after acceptance, before technical editing, formatting and proof reading. Using this free service, authors can make their results available to the community, in citable form, before we publish the edited article. This Accepted Manuscript will be replaced by the edited, formatted and paginated article as soon as this is available.

You can find more information about *Accepted Manuscripts* in the **Information for Authors**.

Please note that technical editing may introduce minor changes to the text and/or graphics, which may alter content. The journal's standard <u>Terms & Conditions</u> and the <u>Ethical guidelines</u> still apply. In no event shall the Royal Society of Chemistry be held responsible for any errors or omissions in this *Accepted Manuscript* or any consequences arising from the use of any information it contains.



Correlation between the chromaticity, dielectric properties and structure of the binary $metal\ pyrophosphates,\ Cu_{(2-x)}Zn_xP_2O_7$

Rattanai Baitahe¹, Naratip Vittayakorn^{1, 2,*} and Santi Maensiri³

¹Electroceramic Research Laboratory, College of Nanotechnology, King Mongkut's Institute of Technology Ladkrabang, Bangkok 10520, THAILAND

²Department of Chemistry, Faculty of Science, King Mongkut's Institute of Technology

Ladkrabang, Bangkok 10520, THAILAND

³School of Physics, Institute of Science, Suranaree University of Technology, Nakhon Ratchasima 30000, THAILAND

*Corresponding author:

Asst. Prof. Dr. Naratip Vittayakorn, Department of Chemistry, Faculty of Science, King Mongkut's Institute of Technology Ladkrabang, Bangkok 10520, THAILAND

E-mail: <u>naratipcmu@yahoo.com</u>

Fax: 66-2-326-4415

Abstract

The binary metal pyrophosphates, $Cu_{(2-x)}Zn_xP_2O_7$; x = 0.50 - 1.50, were synthesized by solid state reaction in order to obtain information on solid solution phase formation. Characteristic peaks of \beta-phase were detected under UV/Vis light emission in the range of 1,200-1,250 cm⁻¹. The P₂O₇⁴⁻ ion, analyzed by vibration, carried the O-P-O radical, P-O-P bridge, and approximate M-O bond stretching, and was identified using Raman and Fourier transform infrared (FT-IR) spectra. The corrected dielectric constant (ε_r) of samples showed a similar value when Cu^{2+} was replaced by Zn^{2+} in the $Cu_2P_2O_7$ structure. However, a slightly decreasing ε_r could still be seen when composition x increased. The color of samples as a function of x = 0.00-1.50 exhibits a greenish hue, except for the composition x = 2.00, which presents a colourless powder. The CIE chromaticity coordinates of $Cu_{(2-x)}Zn_xP_2O_7$; x = 0.50 to 1.50, shifted from (0.303, 0.366) to (0.292, 0.388), thus corresponding to the visible wavelength that shifted from about 506 to 512 nm, and 561 nm for x = 0.00. The phenomena of both dielectric and optical properties resulted from the changing crystal structure of the respective P₂O₇⁴⁻ cluster and octahedral M-O₆ site. Investigation of the crystal structure was carried out by using Rietveld refinement analysis, with support from the extended X-ray absorption fine structure (EXAFS) fitting technique. Furthermore, this study revealed the relationships of binary pyrophosphates between structure and dielectric property, and their correlations to structure and optical property, which were clarified by shrinking chemical bonding, bond angle, number of clusters, and distortion of octahedral MO₆.

Keywords: Binary metal pyrophosphates, Dielectric and optical properties, Structure refinement analysis.

1. Introduction

Generally, the divalent metal pyrophosphate, salt $(M_2P_2O_7; M = metal element)$, has a polymorphic structure. The crystal structure consists of two main parts, which contain six oxygen atoms around a metal atom or octahedral MO₆, and a P₂O₇⁴ cluster that is caused by the polymerization of two $[PO_4]^{3-}$ ions clustering to $[P_2O_7]^{4-\frac{1}{2}}$. These phosphates have two conformed crystallizations. The first is a dichromate type, which shows that the M radius structure is greater than 0.97 Å in, for example, Ca₂P₂O₇, Sr₂P₂O₇, Ba₂P₂O₇, Pb₂P₂O₇, and $\text{Cd}_2\text{P}_2\text{O}_7^{-\frac{3}{2}}$. The $\text{P}_2\text{O}_7^{-4}$ cluster, in eclipsed conformation, crystallizes this group at about the center of the symmetry and P-O-P bridge, which spread towards each other. The second is a thortveitite type, with the M radius of less than 0.97 Å in, for example, Cu₂P₂O₇, Zn₂P₂O₇, Ni₂P₂O₇, Mn₂P₂O₇, Co₂P₂O₇, and Mg₂P₂O₇. This type of P₂O₇⁴ cluster occurs in staggered conformation. On the other hand, the metal pyrophosphate compounds were separated by a stable phase structure at different temperatures, which included α -M₂P₂O₇, and β -M₂P₂O₇ phases (low and high temperature, respectively) $\frac{4}{2}$. Generally, the α -phase is the stability phase of $Cu_2P_2O_7$ at room temperature. The α - $Cu_2P_2O_7$ phase exhibits the monoclinic space group, C2/c, with lattice parameters of a = 6.876 Å, b = 8.113 Å, c = 9.162 Å, and $\beta = 109.54^{\circ}$. A high temperature analysis shows that the monoclinic C2/c transforms to monoclinic C2/m (β - $\text{Cu}_2\text{P}_2\text{O}_7$ phase), with lattice parameters of a = 6.827 Å, b = 8.118 Å, c = 4.576 Å, and $\beta =$ 108.85°. The transition temperature of $\alpha \to \beta$ phase is about 100°C $\frac{5}{2}$. Regarding the Zn₂P₂O₇ structure, α- Zn₂P₂O₇ has the monoclinic space group, I2/c, at room temperature, with unit cell parameters of a = 20.068 Å, b = 8.259 Å, c = 9.099 Å, and $\beta = 106.35^{\circ}$. The transition temperature of α -Zn₂P₂O₇ to β -Zn₂P₂O₇ was found at about 130°C. The β -Zn₂P₂O₇ phase displays the monoclinic space group, C2/m, with unit cell parameters of a = 6.61 Å, b = 8.29 Å, c = 4.51

Å, and $\beta = 105.4^{\circ} \frac{6}{\cdot}$. In addition, the crystal structure of Zn₂P₂O₇ was observed in other phases, such as x and y, which are metastable phases in the form of $2ZnO \cdot P_2O_5^{-\frac{7}{2}}$. The δ - $Zn_2P_2O_7$ phase is a poor crystalline, and the γ -Zn₂P₂O₇ phase is orthorhombic with a unit cell of a = 4.950 Å, b =13.335 Å, and c = 16.482 Å. It is interesting to note that the β -Zn₂P₂O₇ and β -Cu₂P₂O₇ phases have the same space group in the monoclinic phase, which enables the high possibility of solid solution to form at high temperature.

A group of metal pyrophosphate compounds can be applied widely in, for example, biomedical cements, chelating agents, corrosion-resistant coatings, high-quality fertilizers, glass ceramics, and microwave dielectric materials 8-10. Most research studies of this group often focus on synthesis and characterizations $\frac{11}{2}$ such as synthesis by wet chemical processing via metal ammonium phosphate hydrates (MNH₄PO₄·nH₂O) or metal hydrogen phosphate hydrates (MHPO₄·nH₂O) with calcination at different temperatures $\frac{2}{3}$ as follows:

 $M^{2+}_{(aq)} + N H_{4~(aq)}^{~+} + P O_{4~(aq)}^{~3-} \xrightarrow{precipitration} M N H_4 P O_4 n H_2 O_{(s)} \xrightarrow{~~\Delta} M_2 P_2 O_{7(s)} + N H_{3(g)} + n H_2 O_{(g)} \,.$

Kinetics and the thermodynamics of phase formation were studied in order to explain the mechanism of reaction, intermediate reaction, and energy reaction (
$$\Delta H^*$$
, ΔS^* , and ΔG^* , respectively) ¹³⁻¹⁵. In order to understand the crystal structure^{5, 6} and its properties ^{16, 17}, structural refinement of the final product was analyzed. However, the study of relationship between crystal structure and properties has not been performed widely. Therefore, this research aimed to study the relationship between crystal structure and dielectric properties, and that between crystal structure and optical properties of the binary metal pyrophosphates, $Cu_{(2-x)}Zn_xP_2O_7$; $x=0.50$ - 1.50, by using Rietveld refinement analysis and the extended X-ray absorption fine structure (EXAFS) fitting technique. Previously, Kim *et al.* ¹⁸ reported two important factors, which caused polarization in the structure of metal pyrophosphate compounds. These factors contained

shifting O atoms in the collinear P–O–P bridge and movement of M^{2+} ions in the octahedral MO_6 , but with relatively few details of the structure. Consequently, the effect of bond length, bond angle, bond strength, number of P-O-P clusters, average bond length, and distortion of the octahedral MO_6 site were considered in order to explain the relationship between crystal structure, dielectric properties, and optical property of $Cu_{(2-x)}Zn_xP_2O_7$; x=0.00-2.00 metal pyrophosphate compounds, which presented the mechanism of phase formation $\frac{19}{2}$.

2. Experimental procedure

Powders with the compositions, $Cu_{(2-x)}Zn_xP_2O_7$; x = 0.00 - 2.00, were synthesized by solid state reaction using reagent-grade metal oxides and hydrogen phosphate powders of CuO (99.9%), ZnO (99.9%), and (NH₄)₂HPO₄ (99%). All raw materials were weighed at stoichiometric proportion and then mixed homogeneously by vibratory ball milling with stabilized zirconia balls for 24 h in anhydrous ethanol. The dried powders were calcined in crucibles at 800 °C for 24 h, then vibratory-milled again for 2 h. After that, the calcined powder was sieved and mixed with 5 wt.% polyvinyl alcohol (PVA) solution and uniaxial pressed into green disks of 10 mm diameter. The sintering temperature was varied between 700–900 °C for 24 h in order to obtain optimum sintering conditions. In order to eliminate the extrinsic factor of electrical properties such as grain size and density, ceramics with more than 95% theoretical density and near average grain size of each composition were selected for investigating the electrical properties. The vibration group of the samples was examined at room temperature by Fourier transform infrared (FT-IR) spectroscopy in the range of 3000–400 cm⁻¹, with eight scans on a Perkin-Elmer Spectrum GX spectrometer and resolution of 4 cm⁻¹. Raman spectra were measured in the wave number range of 100-1600 cm⁻¹, with eight scans on a Thermo Scientific

DXR Raman microscope, using the 532 nm exciting line of an He-Ne laser in order to support the identification of crystal structured ceramics. The dielectric property was measured at 1 MHz via the use of an LCR meter (HP4284A; Hewlett- Packard, Palo Alto, CA). An image staked SONY IMX214 CMOS sensor collected the colors of the samples, and matched them with CIE chromaticity diagrams in order to approximate the tendency of the absorption wavelength. Details of the crystal structure were studied by X-ray diffraction (XRD) of powder, using a D8 Advanced powder diffractometer (Bruker AXS, Karlsruhe, Germany), with Cu K_{α} radiation (λ = 0.1546 nm); and X-ray absorption spectroscopy (XAS) was conducted on the beam line (BL8) of the National Synchrotron Research Center (Thailand). A double crystal Ge(220) was used for the EXAFS mono-chromator. Transmission mode collected X-ray absorption (XAS) spectra at the Cu and Zn K-edge.

3. Results and discussion

Functional group analysis

FT-IR and Raman spectroscopy (Raman) are powerful methods that analyze the chemical bonding of vibration, rotational, and other low-frequency modes in the phosphate system. $M_2P_2O_7$ is a monoclinic structure with zone-center (C-point) phonons in the lattice vibration of these metal pyrophosphates, and it can be divided by irreducible representation of the spectroscopic group, C_{2h} . Factor group analysis was calculated by using the procedure of Kroumova *et al* 20 . The single metal pyrophosphate, α -Cu₂P₂O₇ (x = 0.00), showed a four formula unit in the unit cell (Z = 4). Cu and P atoms were attributed to the 8f position, and O atoms to both 8f and 4e positions (Wyckoff notation). In order to remove the 3 acoustic modes ($\Gamma_{acoustic} = A_u + 2B_u$) from the total number ($N_{tot} = 66$) of vibrations, the optical modes of lattice

vibration were represented by

$$\Gamma_{\text{optic}} = 16A_{\text{g}} + 15A_{\text{u}} + 17B_{\text{g}} + 15B_{\text{u}}$$

The odd (un-gerade; A_u and B_u) vibration represents infrared-active modes (Γ_{IR}), as presented in the following equation:

$$\Gamma_{\rm IR} = 15A_{\rm u} + 15B_{\rm u}$$

In addition, all even (gerade; A_g and B_g) vibrations are in Raman-active modes (Γ_{Raman}), as exhibited in the following equation:

$$\Gamma_{\text{Raman}} = 16A_{\text{g}} + 17B_{\text{g}}$$

The binary metal pyrophosphates, $Cu_{(2-x)}Zn_xP_2O_7$; x = 0.50, 1.00, and 1.50, showed two formulas in the unit cell (Z = 2). The Cu and Zn atoms distribute in the 4h position, and P atoms are attributed to the 4i position. The O atoms are attributed to three positions that include 2a, 4i, and 8j. IR-active and Raman-active modes, but not acoustic modes, are shown in the following equations:

$$\Gamma_{\rm IR} = 6A_{\rm H} + 9B_{\rm H}$$

$$\Gamma_{\text{Raman}} = 8A_{\text{g}} + 7B_{\text{g}}$$

In addition, the single metal pyrophosphate, α -Zn₂P₂O₇ (x = 2.00), exhibited twelve formulas in the unit cell (Z = 12) that were quite complex in structure. Zn and P atoms were attributed to the 8f position, and O atoms to both 8f and 4e positions. IR-active and Raman-active modes, but not acoustic modes, are determined by the following equations:

$$\Gamma_{\rm IR} = 48A_{\rm u} + 48B_{\rm u}$$

$$\Gamma_{\text{Raman}} = 49A_{\text{g}} + 50B_{\text{g}}$$

As a result, the number of peaks appeared to be more in both FT-IR and Raman spectra of α - $Zn_2P_2O_7$ than in other compounds. A number of peaks were detected in the Raman and IR

techniques that related to the symmetry of crystal structure in pyrophosphate form. This resulted in absorptions of different resonant frequencies by the frequency of absorbed radiation, which matches the transition of energy in the vibrating bond or group. It can be proposed, that bonding in the structure is different, as it appears in many of the peaks. The FT-IR spectra of samples, which closely resemble those of the $M_2P_2O_7$ pyrophosphate group (M = Cu, Cd, Fe, Mn, Ni), are shown in **Figure 1** ^{1, 21}. The strong vibration bands of about 1190 and 1060 cm⁻¹ are attributed to asymmetric (v_{as} PO₃). Vibration bands of about 1100 cm⁻¹ are attributed to symmetric stretching $(v_s PO_3)$ of the PO₃ unit, while asymmetric $(\delta_{as} PO_3)$ and symmetric $(\delta_s PO_3)$ bending vibration is observed at about 584 and 542 cm⁻¹, respectively. The asymmetric (v_{as} P-O-P) and symmetric stretch (v_s P-O-P) bridge vibration for this sample is observed at about 960 and 740 cm⁻¹. respectively. PO₃ determination, rocking mode of P-O-P deformations, and torsional and external modes are found in the 400 cm⁻¹ region. The number of bands in this spectral region confirms the existence of distinct nonequivalent phosphate units in each structure and loss of degeneracy in the vibration modes, which were affected by factor group analysis $\frac{22,23}{2}$. Additionally, a strong (v_s P-O-P) band (730 cm⁻¹) was seen as the FT-IR spectrum of the samples, and is known to be the most striking feature of polyphosphate spectra. Most of the FT-IR data showed details of the functional group of phosphates. Therefore, the support of Raman spectroscopy was used to analyze oxide metal stretching (M-O) and the phase-characteristic (α -, β -phase) of pyrophosphate compounds at low frequencies. The Raman spectra of the samples are shown in Figure 2 and tabulated in Table 1, with FT-IR results affected in the same direction. Furthermore, the Raman results show a β -phase form in pyrophosphate groups $\frac{24}{3}$ by a detectably weak peak of approximately 1,210 cm⁻¹. The single metal pyrophosphates (x = 0.00 and x =2.00), and three distinct peaks that originate from $v_{as}(PO_3)$ vibrations, are visible at about 1210,

1140 and 1080 cm⁻¹. The peaks remain at 1140 and 1080 cm⁻¹ in samples as a function of x =0.50, 1.00, and 1.50, or binary metal pyrophosphates, but they disappear at 1210 cm⁻¹. This indicates that the binary metal phosphates closely resemble those of the β-Cu₂P₂O phase, with a monoclinic structure and the space group, C2/m. In addition, single metal pyrophosphates exhibited an alpha phase (α -phase). The Cu²⁺ ion is replaced by Zn²⁺ in the Cu_(2-x)Zn_(x)P₂O₇ structure. The M-O stretching band of around 200 cm⁻¹ shifts to a lower wave number, and the interatomic distance between the metal and oxygen atom affects bond strength and absorbs energy also at a lower wave number. The single metal pyrophosphates were observed with M–O stretching and peak splitting at 208, 212, and 248 cm⁻¹ for x = 0.00. The sample as a function of x = 2.00 was observed, with five splitting peaks containing 171, 182, 201, 211, and 254. These results show that the sample as a function of x = 2.00 in the crystal structure has a lower symmetry than that of x = 0.00, due to the number of splitting peaks, which causes a different M–O bond length. Regarding binary metal pyrophosphates, splitting peaks were detected in only two regions in each of three samples: 197 and 208 for x = 0.50, 188 and 207 for x = 1.00, and 181 and 206 for x = 1.50. It was pointed out that the crystal structure of binary metal pyrophosphates has more symmetry than single metal pyrophosphate compound, which is proved in the structural analysis of Rietveld refinement and EXASF fitting.

Dielectric and optical properties

The mean static atomic dielectric constant of $Cu_{(2-x)}Zn_xP_2O_7$; x = 0.00 - 2.00 compounds was estimated using the well-known Clausius-Mossotti equation as follows $\frac{25}{3}$:

$$\varepsilon_r = \left(\frac{3V_m + 8\pi\alpha_D}{3V_m - 4\pi\alpha_D}\right)$$

where ε_r is the mean static atomic dielectric constant, α_D is the sum of the dielectric

polarizabilities of individual ions, and $V_{\rm m}$ is the molar volume. Dielectric constant as a function of composition x is presented in **Figure 3**, which shows the comparison between calculated data (red bar), and measurement results (green bar). The single metal pyrophosphates show a dielectric constant of about 13 of ε_r , which is higher than the 10 of ε_r in binary metal pyrophosphates. The Clausius-Mossotti equation focuses on only the dielectric constant from atomic polarization (electron cloud bias in the electric field). Indeed, the samples were measured at 1 MHz frequency for decreasing extrinsic factor, and the polarization caused the cations (Cu²⁺, Zn²⁺, and P⁵⁺) and anions (O²-) in the structure to move. Moving ions in an electric field is the cause of increased dielectric constant over the Clausius-Mossotti equation and calculated data, as considered in this study by bond angle, bond length, and volume of octahedral MO₆.

Color is a property of the coordination complex such as green for $[CoF_6]^{3}$, red for $[Co(NH_3)_5H_2O]^{3+}$, and blue for $[Cu(NH_3)_4H_2O)_2]^{2+}$. The phenomenon of color is explained by the crystal field theory (CFT) $\frac{26, 27}{2}$, from which $Cu_{(2-x)}Zn_xP_2O_7$; x = 0.00 - 2.00 shows a greenish color, except for the composition, x = 2.00, that exhibits a colorless powder. Optical properties and corresponding CIE chromatic coordinates $\frac{26, 28, 29}{2}$ of these samples are demonstrated in Figure 4. Results of the composition, x = 0.00, illustrated a yellowish-green color, while binary metal (x = 0.50 - 1.50) presented color tones that changed from bluish-green to green. The composition, x = 2.00, was seen as colorless. The CIE chromaticity diagram can approximate roughly a visible and an absorption wavelength (nm). The CIE chromaticity coordinates of Cu₍₂₋ $_{x_1}$ Zn_xP₂O₇; x = 0.50 - 1.50 shift from (0.303, 0.366) to (0.292, 0.388) with increasing x, which corresponds to the visible wavelength that shifts from about 506 to 512 nm. The coordinates of α-Cu₂P₂O₇ are (0.3454, 0.4081), which corresponds to a wavelength of about 561 nm. This leads

to octahedral crystal field splitting energy (Δ_0) that illustrates z-axis expansion of the octahedral site, with its length observed by Rietveld refinement analysis and the EXAFS fitting technique. Structure analysis

Structural refinement was performed by the Rietveld refinement analysis ³⁰ using the FULLPROF package $\frac{31}{2}$. A pseudo-Voigt shape function was adequate at all times for obtaining good fits for experimental data. The initial model was taken from parameters in the research of Calvo $\frac{32}{2}$. Factors of the P-O-P bond angle, M-O bond length, and quality of fit (χ^2) were obtained from the Rietveld refinement analysis and are summarized in Table 2. Figure 5 shows the calculated (Y_{cal}) and observed (Y_{obs}) diffraction patterns and different (Y_{obs} -Y_{cal}) peaks of the samples. The plot of refinement gives the evolution of X-ray diffraction (XRD) patterns in various $Cu_{(2-x)}Zn_xP_2O_7$; x = 0.00 - 2.00 compositions, and their synthesized pyrophosphates show that single-phase compounds constitute solid solutions. Similarity in XRD patterns (peak positions) is an indication of only small variations in unit cell parameters, for example, the small difference in size between Cu^{2+} ion (R = 0.73 Å) and Zn^{2+} ion (R = 0.74 Å) $\frac{33}{2}$. Data collected on the Rietveld refinement analysis and XRD of powder confirmed the monoclinic system for the metal pyrophosphate compounds, $Cu_{(2-x)}Zn_{(x)}P_2O_7$; x = 0.00 (space group C^2/c (15), Z = 4), x = 0.000.50 - 1.00 (space group C2/m (12), Z = 2), and x = 2.00 (space group I2/c (15), Z = 12). The relationship between the reflection planes (hkl) of α -Zn₂P₂O₇, α -Cu₂P₂O₇, and Cu_(2-x)Zn_xP₂O₇; x= 0.50 - 1.50 in Figure 5 projects the lattice size. The results show that the crystal structure size of binary metal pyrophosphates is smaller than that of single metal pyrophosphates. Also, the long ordering range of binary metal pyrophosphates is wider than that for single metal pyrophosphates, which were considered as the (111) plane of $Cu_{(2-x)}Zn_xP_2O_7$; x = 0.50 - 1.50, (112) plane of α -Cu₂P₂O₇, and (312) plane of α - Zn₂P₂O₇. Furthermore, the refined data showed

that the space group of Cu₂P₂O₇ increased ordering from the monoclinic system with C2/c to that with C2/m, when Cu^{2+} was replaced by Zn^{2+} in the pyrophosphate structure. The final refinement demonstrated the P-O-P bridge and asymmetry of octahedral MO₆. Furthermore, the P-O-P bond angle was expanded from a linear of 155° to 180°. The calculated number of P-O-P clusters was decreased from 4 to 2 clusters/unit cell, and the number of octahedral MO₆ sites decreased from 8 to 4 sites/unit cell, due to increasing long range ordering and decreasing unit cells, which had a direct effect on electrical properties of matter. The changing M-O bond length in binary metal pyrophosphates was exhibited through the color of matter, which resulted from changing crystal field splitting ²⁶ in the 3d⁹-orbital Cu²⁺ ion, and this was observed in Raman spectroscopy. The relationship between M-O bond length and Raman shift is tabulated in **Table** 3. The Cu^{2+} ion was replaced by Zn^{2+} in the $Cu_{(2-x)}Zn_{(x)}P_2O_7$, which appeared in the M-O stretching band at around 210 cm⁻¹. The stretching band shifted to a lower wave number, due to increasing interatomic distance between the metal and oxygen atom, thus affecting bond strength and energy absorbance. Table 3 shows the band position of M-O bond stretching compared with Rietveld refinement results and approximation of calculated frequencies by fundamental equation. This analysis focused on the tendency of Raman band shift; therefore, the factors used in calculation contained only atomic mass. The results of calculation were obtained in k terms. Each M-O bonding absorbs energy at a different frequency, which brings about a peak in a different position on the Raman shift. The close M-O bond lengths exhibited close peak positions and this developed into an observation band. Thus, the close M-O bond lengths are grouped in Figure 6, with the number of groups corresponding to that of the band in Raman. All of the results are consistent with increasing x compositions that correspond to a decreasing average M-O bond length and decreasing observation frequencies in both Raman shift and

fundamental frequency calculation. In addition, the crystal structure and bonding character of the materials were considered. The average bond strength ($\langle S_{P-O} \rangle$) of P^{5+} and O^{2-} in the $[O3P-O-PO3]^{4-}$ or $[P_2O_7]^{4-}$ cluster and bond valence sum ($\langle V_{P-O} \rangle$) were calculated according to the procedure of Brown $\frac{34}{2}$. The average bond strength (**Table 3**) can be estimated from the average sum of bond valence divided by the average cation coordination numbers, from which bond valence can be defined by

$$V_{P-O} = \exp\left(\frac{R_0 - R}{B}\right)$$

where R is the length of a bond between P and O atoms. R_0 and B are parameters determined empirically, by which the B parameter must use a universal value for the empirical parameter B; B = 0.37 Å, which makes a one-parameter model relating to the formal valence V, bond length R, and coordination number N. Therefore, the sum of the bond valence is defined by

$$V_i = \sum_{j}^{N} \exp\left(\frac{(R_1 - R_{ij})}{0.37}\right)$$

In divergence, the average bond strength of a single metal pyrophosphate is smaller than that in binary metal pyrophosphates. Bond energies and force constants decrease with average bond strength. Determination of a quantitative correlation in the same type of bonding is complex ³⁵. The EXAFS fitting technique was used in support of the structural refinement analysis.

The EXAFS spectra of the samples for the Cu K-edge and Zn K-edge are shown in **Figures 7a** and **7b**, respectively. In order to study the environment around Cu atoms, a primitive EXAFS model was taken from parameters obtained from the Rietveld refinement of each sample. The details of EXAFS spectroscopic fitting are summarized in **Table 4**. The results exhibited distortion of octahedral CuO₆. The sample as a function of x = 0.00 showed three main shells, of which the first shell of the spectrum was modeled in consistence with four oxygen

atoms that had interatomic distances of 1.9050 Å and 1.9643 Å for Cu-O1 and Cu-O2, respectively. Then, the second shell detected only one oxygen atom; Cu-O3, which had an interatomic distance of 2.3001 Å. The last shell detected the oxygen atom of octahedral CuO₆ which had an interatomic distance of 2.9136 Å that combined a scattering phosphorus atom. Cu-P and metal cupper atom, as well as Cu–M interaction. In the case of binary metal pyrophosphate samples (x = 0.50 - 1.50), the Cu–O3 interatomic distances shortened, and were included in the second shell. As a result, the second shell intensity of the binary metal pyrophosphate samples was seen to be higher than that in $Cu_2P_2O_7$ (x = 0.00). The addition of a fourth shell did not improve the quality of fit, and fitting of the Zn K-edge EXAFS was related to that of the Cu Kedge, with the curve shifting to a high radial distance due to a larger atomic radius. The EXAFS spectrum of Zn-O is shown by a single oscillation from four oxygen atoms surrounding the central Zn atom in the first shell, while Zn consists of two oxygen atoms in the second shell. The next shell described the combination of Cu-M (M = Cu/Zn), and Cu-P interaction. The difference in radial distances between Rietveld refinement and EXAFS fitting may be caused by the type of measurement in each technique, in which X-ray diffraction investigated the global structure, and X-ray absorption probed into details of the Cu/Zn local structure 36, 37. The fitting statistic (R-factor) of the Zn K-edge is worse than that of the Cu K-edge because of two factors. Firstly, the crystal structure of α-Zn₂P₂O₇ showed lower symmetry when compared with other samples, and Zn exhibited three different types of atomic position in the unit cell. Secondly, there was a limitation in the instrument, in which the absorption edge of Zn (9659 eV) approached the maximum energy range (1,250 – 10,000 eV) of the BL8 station.

The refinement results by P-O-P bond angle can be classified into two groups. The first group includes a P-O-P bond angle of less than 180° such as the compositions, x = 0.00 and x = 0.00

2.00, or single metal pyrophosphates. The sample as a function of x = 0.00 had a P-O-P bond angle of 154.6°, and appeared with 4 clusters/unit cell and symmetric P-O bond lengths of 1.574 Å. The composition, x = 2.00, showed two different P-O-P bond angles, including 159.0°, which appeared with 8 clusters/unit cell and asymmetric P-O bond lengths of 1.770 Å and 1.390 Å, and the P-O-P bond angle of 138.0° appeared with 4 clusters/unit cell and a symmetric P-O bond length of 1.640 Å. The second group had a P-O-P bond angle equal to 180°, which contained the compositions, x = 0.50, 1.00, and 1.50, or binary metal pyrophosphates. All of the compositions in this group exhibited a P-O-P bond angle equal to 180.0° and appeared with 4 clusters/unit cell and symmetric P–O bond lengths of 1.524 Å, 1.521 Å, and 1.519 Å for x = 0.50, 1.00, and 1.50, respectively. However, when compared to an equal space volume, the number of P-O-P clusters in each composition was equal. As a result, the number of P-O-P clusters did not affect the polarization of samples. The single metal pyrophosphates showed an outstanding dielectric constant, while all binary metal pyrophosphates presented lower and similar dielectric constants. It was highly possible that high polarization caused a narrow P-O-P bond angle, as analyzed through the dielectric constant of metal pyrophosphate compound. In addition, the long P-O bond length of x = 2.00 (weak bonding) led to better polarization of x = 0.00, 0.50, 1.00, and 1.50. The binary metal pyrophosphates (x = 0.50, 1.00, and 1.50) exhibited a close dielectric constant, due to all the P-O-P bond angles being equal. However, the dielectric constant tends to decrease slightly when the composition, x, increases. Results from the final refinement showed decreasing average M–O bond lengths in the octahedral MO₆ site, of which short length bonding caused hard polarization. Additionally, the volume of selected octahedral coordination was calculated by the Swanson et al. method $\frac{38}{2}$ for promoting the relationship between polarization and metal oxide bonding. In addition, the distortion index used promotion simultaneously. Baur $\frac{39}{2}$ described D based on bond lengths in the distortion index as

$$D = \frac{1}{n} \sum_{i=1}^{n} \frac{\left| l_i - l_{av} \right|}{l_{av}}$$

where l_{av} is the average bond length, and l_i is the atomic distance from the central atom to the *i*th coordinating atom. These results are tabulated in **Table 5**. All data included decreasing average bond lengths, octahedral volume and the distortion index, which exhibited decreasing polarization (dielectric constant, ε_r) when the composition, x, increased. These analyses show that polarization of the $Cu_{(2-x)}Zn_xP_2O_7$; x = 0.00 - 2.00 system occurred from two factors, with shifting O atoms in the collinear P–O–P bridge probably being the main factor in a narrow bond angle that causes high polarization and a high dielectric constant. The movement of M²⁺ ions in the octahedral MO₆ is a supplementary factor, in which the longer average M–O bond length and larger octahedral volume lead to high polarization and a high dielectric constant of metal pyrophosphate compounds.

The distortion of octahedral CuO_6 exhibited decreasing Cu-O3 bond lengths from x =0.00 to 1.50, which corresponded to decreasing octahedral crystal field splitting energy (Δ_0). As a result, Zn²⁺ increased when the Cu²⁺ in Cu₂P₂O₇ compound was replaced. The color of compounds illustrated that its hue changes from bluish-green to green. The colorless composition, x = 2.00 or $Zn_2P_2O_7$, caused a state of fulfillment in the octet rule of Zn^{2+} ions ([Ar] 3d¹⁰) in the structure, despite distortion appearing in the octahedral ZnO₆ site. The octahedral splitting diagram of $Cu_{(2-x)}Zn_xP_2O_7$; x = 0.00 - 1.50 is shown and summarized in **Figure 8**. Total interpretations showed that distorted octahedral MO₆ affects both the color of matter and polarization of the octahedral unit, as reflected by the dielectric constant.

4. Conclusion

The single metal pyrophosphates, α -Cu₂P₂O₇ and α -Zn₂P₂O₇, and binary metal pyrophosphates, $Cu_{(2-x)}Zn_xP_2O_7$; x = 0.00 - 1.50, were synthesized successfully by solid state reaction from metal oxide and ammonium hydrogen phosphate. All of the samples exhibited a single-phase monoclinic system with the C2/c space group for α -Cu₂P₂O₇ and α -Zn₂P₂O₇ (I2/c), and C2/m space group for binary metal pyrophosphates, which showed that the binary metal had more symmetry in structure than single metal pyrophosphates. Rietveld refinement and EXAFS fitting data presented the P-O-P bond angle and P-O bond length in P₂O₇⁴⁻ ions, and also details of octahedral MO₆ containing the average bond length, octahedral volume, and distortion index. The addition of Zn²⁺ ions in the Cu₂P₂O₇ structure caused distortion of the crystal structure. which led to a change in the bond length and bond angle of the P-O-P clusters in $P_2O_7^{4-}$ ions. and changed the octahedral volume and average bond lengths of the octahedral MO₆ site. Shifting O atoms in the collinear P–O–P bridge is probably the main factor in ionic polarization, in which a narrow bond angle caused high polarization and high dielectric constant. The movement of M²⁺ ions in octahedral MO₆ is a supplementary factor, in which the longer average M–O bond length and larger octahedral volume led to the high polarization and high dielectric constant of metal pyrophosphate compounds. The color of samples changed from bluish-green to green when the Zn composition increased because the wavelength of absorption increased and corresponded to the decrease in z-axis expansion. The final results showed that the distortion of octahedral MO₆ caused a direct effect on the color of metal pyrophosphate compounds, while the change of P–O–P bridge affected dielectric properties.

Acknowledgements

This work was supported by the Thailand Research Fund (TRF) under the TRF Senior Research Scholar, Grant no RTA5680008 and The National Nanotechnology Center (NANOTEC), NSTDA, Ministry of Science and Technology, Thailand, through its program of Center of Excellence Network. The authors also would like to thank the Synchrotron Light Research Institute (Public Organization) for the XAS measurement.

5. References

- 1. E. Steger and B. Käßner, *Spectrochimica Acta Part A: Molecular Spectroscopy*, 1968, **24**, 447-456.
- 2. B. Boonchom and R. Baitahe, *Materials Letters*, 2009, **63**, 2218-2220.
- 3. M. Weil and B. Stöger, *Acta Crystallographica Section B: Structural Science*, 2010, **66**, 603-614.
- 4. A. Durif, Crystal chemistry of condensed phosphates, Plenum Press, New York, 1995.
- 5. B. E. Robertson and C. Calvo, *Acta Crystallographica*, 1967, **22**, 665-672.
- 6. C. Calvo, Canadian Journal of Chemistry, 1965, **43**, 1147-1153.
- 7. M. A. Petrova, V. I. Shitova, G. A. Mikirticheva, V. F. Popova and A. E. Malshikov, *Journal of Solid State Chemistry*, 1995, **119**, 219-223.
- 8. J. I. Bian, D. W. Kim and K. S. Hong, *Jpn J Appl Phys 1*, 2004, **43**, 3521-3525.
- 9. J. J. Bian, D. Kim and K. S. Hong, *J Mater Sci*, 2005, **40**, 1801-1803.
- 10. W. Wenwei, F. Yanjin, W. Xuehang, L. Sen and L. Shushu, *Journal of Physics and Chemistry of Solids*, 2009, **70**, 584-587.
- 11. Z. W. Xiao, G. R. Hu, Z. D. Peng, K. Du and X. G. Gao, Chinese Chemical Letters, 2007,

- **18**, 1525-1527.
- 12. A. Bensalem, M. Ahluwalia, T. V. Vijayaraghavan and Y. H. Ko, *Materials Research Bulletin*, 1997, **32**, 1473-1483.
- D. Brandová, M. Trojan, M. Arnold, F. Paulik and J. Paulik, *Journal of Thermal Analysis*,
 1988, 34, 1449-1454.
- D. Brandová, M. Trojan, F. Paulik and J. Paulik, *Journal of Thermal Analysis*, 1987, 32, 1923-1928.
- 15. B. Boonchom, R. Baitahe, S. Kongtaweelert and N. Vittayakorn, *Industrial & Engineering Chemistry Research*, 2010, **49**, 3571-3576.
- A. Jouini, J. C. Gâcon, M. Ferid and M. Trabelsi-Ayadi, *Optical Materials*, 2003, 24, 175-180.
- 17. T. Yang and J. Lin, *Journal of Solid State Chemistry*, 2013, **198**, 1-5.
- 18. C. H. Kim and H. S. Yim, *Solid State Communications*, 1999, **110**, 137-142.
- 19. R. Baitahe and N. Vittayakorn, *Thermochimica Acta*, 2014, **596**, 21-28.
- 20. E. Kroumova, M. I. Aroyo, J. M. Perez-Mato, A. Kirov, C. Capillas, S. Ivantchev and H. Wondratschek, *Phase Transitions*, 2003, **76**, 155-170.
- 21. B. Boonchom and N. Phuvongpha, *Materials Letters*, 2009, **63**, 1709-1711.
- 22. O. Pawlig and R. Trettin, *Materials Research Bulletin*, 1999, **34**, 1959-1966.
- 23. O. Pawlig, V. Schellenschläger, H. D. Lutz and R. Trettin, *Spectrochimica Acta Part A: Molecular and Biomolecular Spectroscopy*, 2001, **57**, 581-590.
- K. Pogorzelec-Glaser, A. Pietraszko, B. Hilczer and M. Polomska, *Phase Transitions*,
 2006, 79, 535-544.
- 25. M. T. Sebastian, Dielectric materials for wireless communication, Elsevier, Amsterdam;

- Boston, 2008.
- 26. A. El Jazouli, B. Tbib, A. Demourgues and M. Gaudon, *Dyes and Pigments*, 2014, **104**, 67-74.
- 27. L.-T. Chen, C.-S. Hwang, I. L. Sun and I.-G. Chen, *Journal of Luminescence*, 2006, 118, 12-20.
- 28. B. Kukliński, D. Wileńska, S. Mahlik, K. Szczodrowski, M. Grinberg and A. M. Kłonkowski, *Optical Materials*, 2014, **36**, 633-638.
- 29. B.-K. Kim and R.-H. Park, *Image and Vision Computing*, 2010, **28**, 952-964.
- 30. H. Rietveld, Journal of Applied Crystallography, 1969, 2, 65-71.
- 31. J. Rodríguez-Carvajal, *Physica B: Condensed Matter*, 1993, **192**, 55-69.
- 32. B. E. Robertson and C. Calvo, Canadian Journal of Chemistry, 1968, 46, 605-612.
- 33. R. Shannon, Acta Crystallographica Section A, 1976, **32**, 751-767.
- 34. I. Brown, Acta Crystallographica Section B, 1977, 33, 1305-1310.
- 35. I. Brown, Acta Crystallographica Section B, 1992, 48, 553-572.
- 36. V. I. Voronin, I. F. Berger, V. A. Cherepanov, L. Y. Gavrilova, A. N. Petrov, A. I. Ancharov, B. P. Tolochko and S. G. Nikitenko, Nuclear Instruments and Methods in Physics Research Section A: Accelerators, Spectrometers, Detectors and Associated Equipment, 2001, 470, 202-209.
- 37. Y. L, B. Huliyageqi, W. Haschaolu, Z. Song, O. Tegus and I. Nakai, *Journal of Electron Spectroscopy and related Phenomena*, 2014, **196**, 104-109.
- 38. D. K. Swanson and R. C. Peterson, *The Canadian Mineralogist*, 1980, **18**, 153-156.
- 39. W. Baur, *Acta Crystallographica Section B*, 1974, **30**, 1195-1215.

Table Headings

- **Table 1** Vibrational assignment of the samples
- **Table 2** Bond angle and bond length from Rietveld refinement for samples
- **Table 3** The approximate grouping of M-O bonding and bond strength of samples
- **Table 4** Bond length from EXAFS fitting for samples
- **Table 5** The evolution of average bond length, octahedral volume, and distortion index of samples
- **Table 6** Approximate wavelength of energy absorption

Figure Legends

- **Figure 1** FT-IR spectra of $Cu_{(2-x)}Zn_xP_2O_7$; x = 0.00 2.00.
- **Figure 2** Raman spectra of $Cu_{(2-x)}Zn_xP_2O_7$; x = 0.00 2.00.
- **Figure 3** Dielectric constant plots of $Cu_{(2-x)}Zn_xP_2O_7$; x = 0.00 2.00.
- **Figure 4** CIE chromatic coordinates of $Cu_{(2-x)}Zn_xP_2O_7$; x = 0.00 2.00.
- **Figure 5** Rietveld refinement patterns of $Cu_{(2-x)}Zn_xP_2O_7$; x = 0.00 2.00.
- **Figure 6**. The approximate grouping of M-O bonding of $Cu_{(2-x)}Zn_xP_2O_7$; x = 0.00 2.00.
- **Figure 7** EXAFS fitting curves of $Cu_{(2-x)}Zn_xP_2O_7$; x = 0.00 2.00.
- **Figure 8** Summary of crystal field splitting in $Cu_{(2-x)}Zn_xP_2O_7$; x = 0.00 1.50.

Table 1

Wave number (cm ⁻¹)	FT-IR	Raman	Assignment
1250 - 1200	-	W	α-phase characteristic
1200 - 1100	VS	VS	$\nu_{as}(PO_3)$
1100 - 1050	VS	VS	$\nu_{\rm s}({ m PO_3})$
1050 - 1000	VS	VS	$\nu_{as}(PO_3)$
980 - 950	S	VW	$\nu_{as}(POP)$
760 - 730	m	\mathbf{W}	$\nu_{\rm s}({\rm POP})$
650 - 280	S	S	$\delta(OPO) + \nu(M-O)$
160 - 260	-	\mathbf{W}	$\nu(M-O)$
200-100	-	m	lattice vibration

vw: very weak, w: weak, m: medium, s: strong, vs: very strong

Table 2

Sam	ple	x = 0.00	x = 0.50	x = 1.00	x = 1.50	x = 2.00		
POP An	gle (°)	154.6	180.0	180.0	180.0	138.00	138.00 159.00	
	,	(10)	(11)	(11)	(11)	(30)	(30))
	M-O1	1.980	2.016	2.037	2.047	3.135	2.196	1.976
		(5)	(2)	(6)	(7)	(15)	(11)	(11)
M-O	M-O2	1.942	1.971	2.012	1.999	1.997	2.017	2.010
bond		(6)	(4)	(5)	(2)	(13)	(11)	(12)
length	M-O3	1.886	2.540	2.476	2.422	2.052	2.371	1.920
(Å)		(5)	(2)	(3)	(3)	(13)	(16)	(11)
	M-O3	2.920	2.540	2.476	2.422	2.181	2.079	2.102
		(9)	(2)	(3)	(3)	(15)	(11)	(14)
Space g	group	C2/c	C2/m	C2/m	C2/m		<i>I</i> 2/ <i>c</i>	
Z		4	2	2	2		12	
χ^2		1.21	1.21	1.33	1.58		1.6	
-	- (Å)	6.8811	6.7904	6.7257	6.6672		20.1098	
	a (Å)	(4)	(3)	(3)	(4)		(6)	
	h (Å)	8.1173	8.1576	8.1986	8.2413		8.2732	
	<i>b</i> (Å)	(4)	(3)	(3)	(4)		(2)	
Lattice	a (Å)	9.1614	4.5579	4.54312	4.5307		9.1067	
	c (Å)	(5)	(2)	(3)	(3)		(3)	
parameter	ρ (9)	109.523	108.429	107.464	106.473	106.326		
	β (°)	(3)	(2)	(3)	(3)		(2)	
$V(\text{Å}^3)$	482.308	239.538	238.971	238.733		1454.012		
	V (A)	$V(\mathbf{A})$ (43)	(17)	(24)	(27)		(74)	
	R _p	9.27	10.0	11.50	14.20		15.70	
R-factor (%)	R_{wp}	11.70	12.70	14.40	17.90		23.10	
(70)	R_{exp}	10.68	11.57	13.49	14.43		18.27	

Table 3

Composition	Observed	(1)	(2)	(3)	(4)	(5)	
	Ra (cm ⁻¹)	-	_	208	212	248	
– 0.00	Avg D (Å)	_	-	1.886	1.961	2.92	
x = 0.00	Cal.		203.72k				
	<s<sub>P-O></s<sub>		1.1232				
	Ra (cm ⁻¹)	-	197	208	-	-	
x = 0.50	Avg D (Å)	-	1.994	2.54	-	-	
x - 0.50	Cal.		203.57k				
	$< S_{P-O} >$		1.2840				
	Ra (cm ⁻¹)	-	188	207	-	-	
x = 1.00	Avg D (Å)	-	2.024	2.476	-	-	
x - 1.00	Cal.	203.42k					
	$< S_{P-O} >$			1.2938			
	Ra (cm ⁻¹)	-	181	206	-	-	
x = 1.50	Avg D (Å)	-	2.023	2.422	-	-	
x - 1.30	Cal.	203.28k					
	$< S_{P-O} >$			1.3011			
	Ra (cm ⁻¹)	171	182	201	211	254	
x = 2.00	Avg D (Å)	1.976	2.033	2.188	2.371	3.135	
	Cal.	203.14k					
	$< S_{P-O} >$	> 1.0969					

Ra: Raman shift (cm⁻¹) Avg D: Average atomic distance (Å)

Table 4

$ \begin{array}{c ccccccccccccccccccccccccccccccccccc$							
0.00	Composition (x)	Path	Shell	CN	R (Å)	$\sigma^2 (\mathring{A}^2)$	R-factor
Cu-O3 2 1 2.30075 0.03223 0.00369 Cu-O3 3 1 2.91358 0.00796 Cu-O1 1 2 1.93460 0.00775 Cu-O2 1 2 1.97180 0.00996 0.00519 Cu-O3 2 2 2.32395 0.02004 Zn-O1 1 2 1.98304 0.02336 Zn-O2 1 2 2.02117 0.00034 0.01175 Zn-O3 2 2 2.38214 0.03426 Cu-O1 1 2 1.93087 0.00575 Cu-O2 1 2 1.97205 0.00647 0.00514 Cu-O3 2 2 2.28269 0.02209 Zn-O1 1 2 1.98889 0.02117 0.00647 0.00647 Zn-O3 2 2 2.35128 0.07393 0.01085 0.007393 0.00611 0.00611 0.00611 0.00763 0.00611 0.00763 0.00763 0.00763 0.00763 0.00763 0.00763 0.00763 0.00763		Cu-O1	1	2	1.90505	0.00508	
Cu-O3 2 1 2.30075 0.03223 Cu-O3 3 1 2.91358 0.00796 Cu-O1 1 2 1.93460 0.00775 Cu-O2 1 2 1.97180 0.00996 0.00519 Cu-O3 2 2 2.32395 0.02004 Zn-O1 1 2 1.98304 0.02336 Zn-O2 1 2 2.02117 0.00034 0.01175 Zn-O3 2 2 2.38214 0.03426 Cu-O1 1 2 1.93087 0.00575 Cu-O2 1 2 1.97205 0.00647 0.00514 Cu-O2 1 2 1.98889 0.02107 Zn-O1 1 2 1.98889 0.02117 Zn-O2 1 2 2.03131 0.00406 0.01085 Zn-O3 2 2 2.35128 0.07393 Cu-O1 1 2 1.94951 0.00611 Cu-O2 1 2 1.99453 0.25154 0.00763 Cu-O3 2 2 2.26768 0.0392 Zn-O1 1 2 2.00714 0.01068 Zn-O2 1 2 2.05349 0.01074 0.00393 Zn-O3 2 2 2.33473 0.04422 Zn-O1 1 2 1.96928 0.00176 Zn-O2 1 2 1.96928 0.00176 Zn-O2 1 2 1.96928 0.00176 Zn-O2 1 2 2.05357 0.00823 Zn-O1 1 2 1.96928 0.00176 Zn-O2 1 2 2.05357 0.00823 Zn-O1 1 2 2.05357 0.00823 Zn-O2 1 2 2.05357 0.00823 Zn-O2 1 2 2.05357 0.00823 Zn-O2 1 2 2.05357 0.00823 Zn-O3 2 1 2.11171 0.00931	0.00	Cu-O2	1	2	1.96427	0.00499	0.00360
Cu-O1 1 2 1.93460 0.00775 Cu-O2 1 2 1.97180 0.00996 0.00519 Cu-O3 2 2 2 2.32395 0.02004 Zn-O1 1 2 1.98304 0.02336 Zn-O2 1 2 2.02117 0.00034 0.01175 Zn-O3 2 2 2.38214 0.03426 Cu-O1 1 2 1.93087 0.00575 Cu-O2 1 2 1.97205 0.00647 0.00514 Cu-O3 2 2 2.28269 0.02209 Zn-O1 1 2 1.98889 0.02117 Zn-O2 1 2 2.03131 0.00406 0.01085 Zn-O3 2 2 2.35128 0.07393 Cu-O1 1 2 1.94951 0.00611 Cu-O2 1 2 1.94953 0.25154 0.00763 Zn-O1 1 2 2.00714 0.01068 Zn-O2 1 2 2.05349 0.01074 0.00393 Zn-O3 2 2 2.33473 0.04422 Zn-O1 1 2 1.96928 0.00176 Zn-O3 2 1 2 2.05357 0.00823 Zn-O1 1 2 1.96928 0.00176 Zn-O3 2 1 2 2.05357 0.00823 Zn-O2 1 2 2.05357 0.00823 Zn-O3 2 1 2.11171 0.00931	0.00	Cu-O3	2	1	2.30075	0.03223	0.00309
Cu-O2 1 2 1.97180 0.00996 0.00519 Cu-O3 2 2 2.32395 0.02004 Zn-O1 1 2 1.98304 0.02336 Zn-O2 1 2 2.02117 0.00034 0.01175 Zn-O3 2 2 2.38214 0.03426 Cu-O1 1 2 1.93087 0.00575 Cu-O2 1 2 1.97205 0.00647 0.00514 Cu-O2 1 2 1.97205 0.00647 0.00514 Zn-O1 1 2 1.98889 0.02117 Zn-O2 1 2 2.03131 0.00406 0.01085 Zn-O3 2 2 2.35128 0.07393 Cu-O1 1 2 1.94951 0.00611 Cu-O2 1 2 1.94951 0.00611 Cu-O3 2 2 2.26768 0.0392 Zn-O1 1 2 2.00714		Cu-O3	3	1	2.91358	0.00796	
0.50		Cu-O1	1	2	1.93460	0.00775	
Zn-O1		Cu-O2	1	2	1.97180	0.00996	0.00519
Zn-O1	0.50	Cu-O3	2	2	2.32395	0.02004	
Zn-O3 2 2 2.38214 0.03426	0.50	Zn-O1	1	2	1.98304	0.02336	
Cu-O1 1 2 1.93087 0.00575 Cu-O2 1 2 1.97205 0.00647 0.00514 Cu-O3 2 2 2.28269 0.02209 Zn-O1 1 2 1.98889 0.02117 Zn-O2 1 2 2.03131 0.00406 0.01085 Zn-O3 2 2 2.35128 0.07393 Cu-O1 1 2 1.94951 0.00611 Cu-O2 1 2 1.99453 0.25154 0.00763 Cu-O3 2 2 2.26768 0.0392 Zn-O1 1 2 2.00714 0.01068 Zn-O2 1 2 2.05349 0.01074 0.00393 Zn-O3 2 2 2.33473 0.04422 Zn-O1 1 2 1.96928 0.00176 2.00 Zn-O2 1 2 1.96928 0.00176 2.00 Zn-O2 1 2 2.05357 0.00823 Zn-O3 2 1 2.11171 0.00931		Zn-O2	1	2	2.02117	0.00034	0.01175
1.00		Zn-O3	2	2	2.38214	0.03426	
1.00		Cu-O1	1	2	1.93087	0.00575	
Zn-O1		Cu-O2	1	2	1.97205	0.00647	0.00514
Zn-O1 1 2 1.98889 0.02117 Zn-O2 1 2 2.03131 0.00406 0.01085 Zn-O3 2 2 2.35128 0.07393 Cu-O1 1 2 1.94951 0.00611 Cu-O2 1 2 1.99453 0.25154 0.00763 Cu-O3 2 2 2.26768 0.0392 Zn-O1 1 2 2.00714 0.01068 Zn-O2 1 2 2.05349 0.01074 0.00393 Zn-O3 2 2 2.33473 0.04422 Zn-O1 1 2 1.96928 0.00176 2.00 Zn-O2 1 2 2.05357 0.00823 Zn-O3 2 1 2.11171 0.00931	1.00	Cu-O3	2	2	2.28269	0.02209	
Zn-O3 2 2 2.35128 0.07393	1.00	Zn-O1	1	2	1.98889	0.02117	
Cu-O1 1 2 1.94951 0.00611 Cu-O2 1 2 1.99453 0.25154 0.00763 Cu-O3 2 2 2.26768 0.0392 Zn-O1 1 2 2.00714 0.01068 Zn-O2 1 2 2.05349 0.01074 0.00393 Zn-O3 2 2 2.33473 0.04422 Zn-O1 1 2 1.96928 0.00176 Zn-O2 1 2 2.05357 0.00823 Zn-O3 2 1 2.11171 0.00931		Zn-O2	1	2	2.03131	0.00406	0.01085
Cu-O2 1 2 1.99453 0.25154 0.00763 Cu-O3 2 2 2.26768 0.0392 Zn-O1 1 2 2.00714 0.01068 Zn-O2 1 2 2.05349 0.01074 0.00393 Zn-O3 2 2 2.33473 0.04422 Zn-O1 1 2 1.96928 0.00176 Zn-O2 1 2 2.05357 0.00823 Zn-O3 2 1 2.11171 0.00931		Zn-O3	2	2	2.35128	0.07393	
1.50		Cu-O1	1	2	1.94951	0.00611	
Zn-O1 1 2 2.00714 0.01068 Zn-O2 1 2 2.05349 0.01074 0.00393 Zn-O3 2 2 2.33473 0.04422 Zn-O1 1 2 1.96928 0.00176 Zn-O2 1 2 2.05357 0.00823 Zn-O3 2 1 2.11171 0.00931		Cu-O2	1	2	1.99453	0.25154	0.00763
Zn-O1 1 2 2.00714 0.01068 Zn-O2 1 2 2.05349 0.01074 0.00393 Zn-O3 2 2 2.33473 0.04422 Zn-O1 1 2 1.96928 0.00176 Zn-O2 1 2 2.05357 0.00823 Zn-O3 2 1 2.11171 0.00931	1.50	Cu-O3	2	2	2.26768	0.0392	
Zn-O3 2 2 2.33473 0.04422 Zn-O1 1 2 1.96928 0.00176 Zn-O2 1 2 2.05357 0.00823 0.02072 Zn-O3 2 1 2.11171 0.00931		Zn-O1	1	2	2.00714	0.01068	
Zn-O1 1 2 1.96928 0.00176 Zn-O2 1 2 2.05357 0.00823 0.02072 Zn-O3 2 1 2.11171 0.00931		Zn-O2	1	2	2.05349	0.01074	0.00393
2.00 Zn-O2 1 2 2.05357 0.00823 0.02072 Zn-O3 2 1 2.11171 0.00931		Zn-O3	2	2	2.33473	0.04422	
Zn-O3 2 1 2.11171 0.00931 0.02072	2.00	Zn-O1	1	2	1.96928	0.00176	
Zn-O3 2 1 2.11171 0.00931		Zn-O2	1	2	2.05357	0.00823	0.02072
Zn-O3 3 1 2.58544 0.06587				_			0.02072
		Zn-O3	3	1	2.58544	0.06587	

Composition (x)	Average bond length (Å)	Octahedral volume (ų)	Distortion index
0.50	2.1758	12.6629	0.1117
1.00	2.1720	12.5791	0.0935
1.50	2.1659	12.4106	0.0821

Table 6

Composition	Wavelength (nm)		$\Delta_{ m o}$	Cu-O3 (Å) bond length	
(x)	Observed	Absorbed	(kJ/mol)	XRD	EXAFS
0.00	561	403	297	2.92	2.91
0.50	506	660	181	2.54	2.32
1.00	508	665	180	2.48	2.28
1.50	512	675	177	2.42	2.27
2.00	-	-	-	-	-

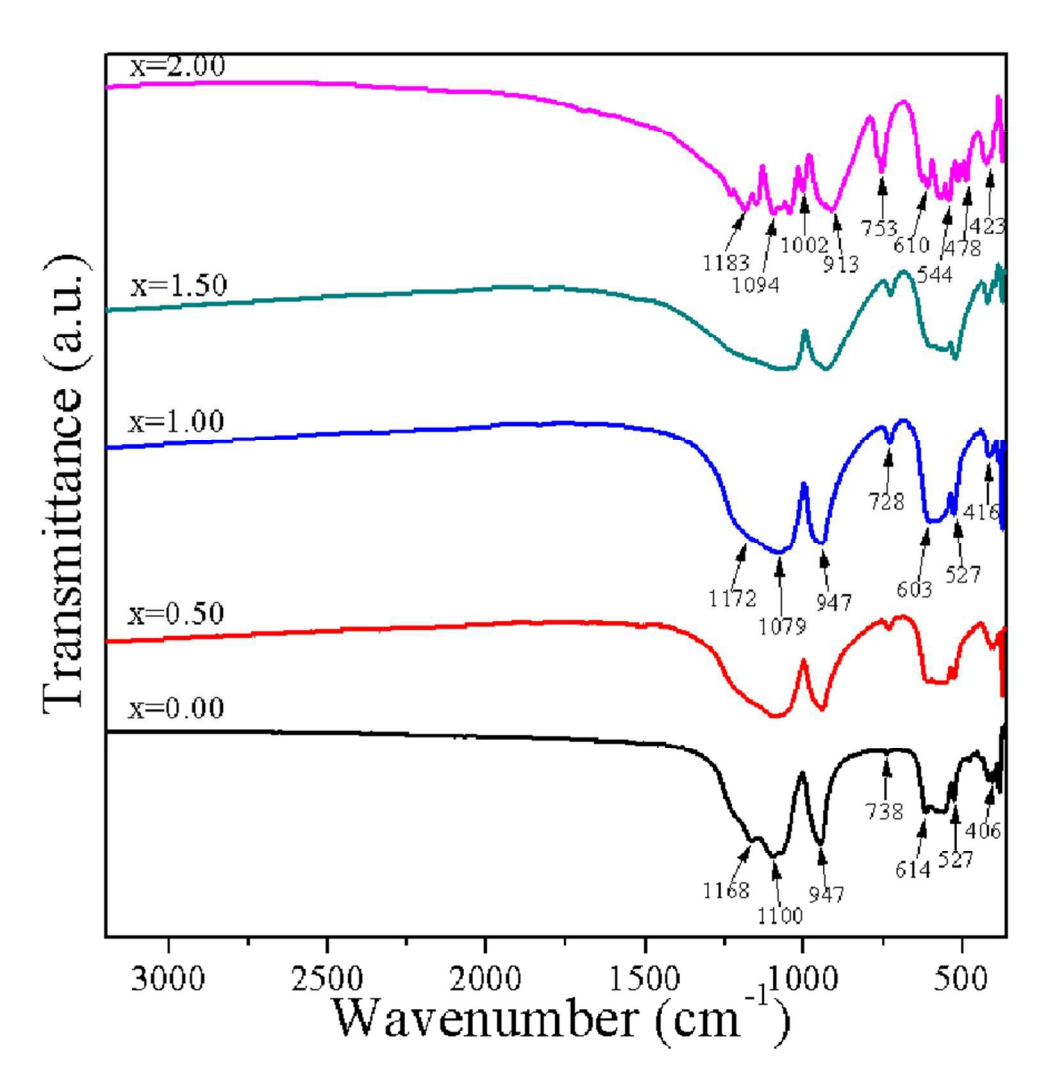


Figure 1 FT-IR spectra of Cu(2-x)ZnxP2O7 ; x = 0.00 - 2.00. 76x78mm (300 x 300 DPI)

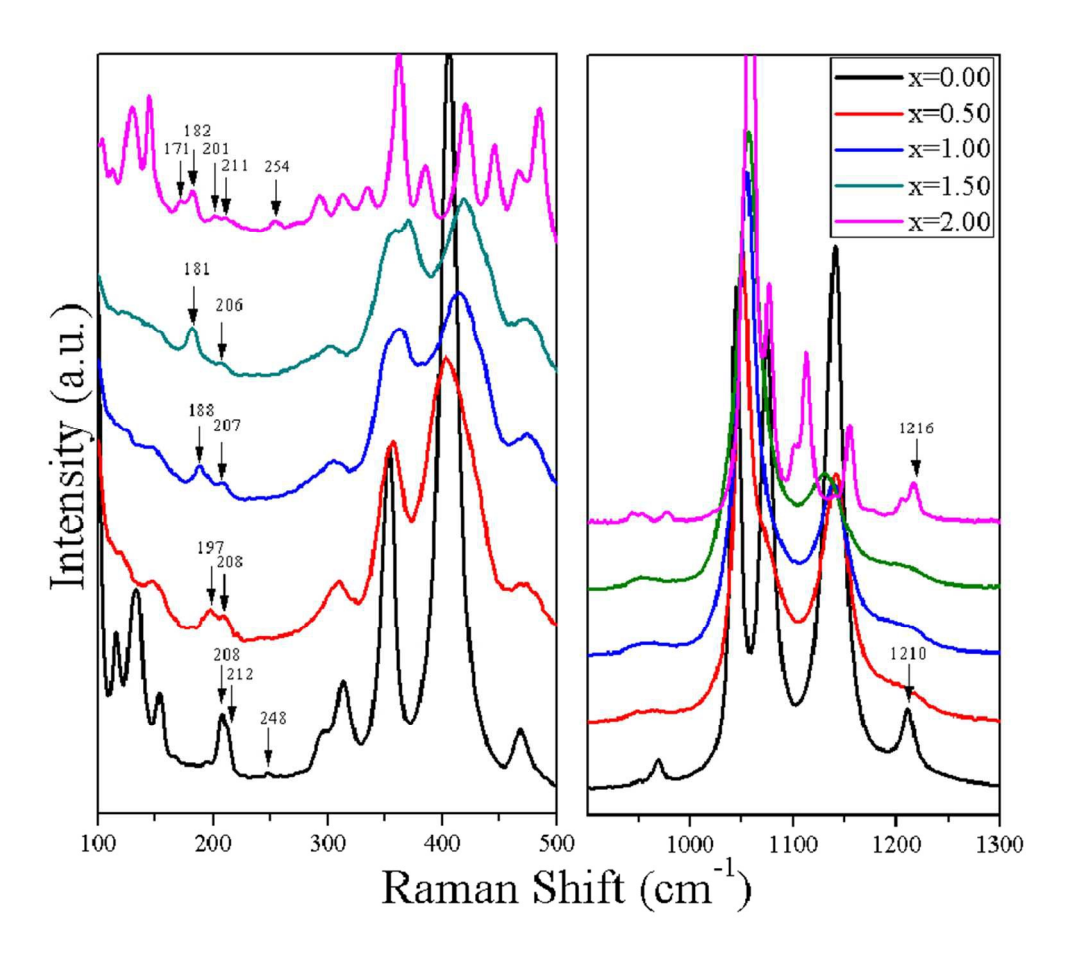


Figure 2 Raman spectra of Cu(2-x)ZnxP2O7 ; x = 0.00 - 2.00. 76x67mm (300 x 300 DPI)

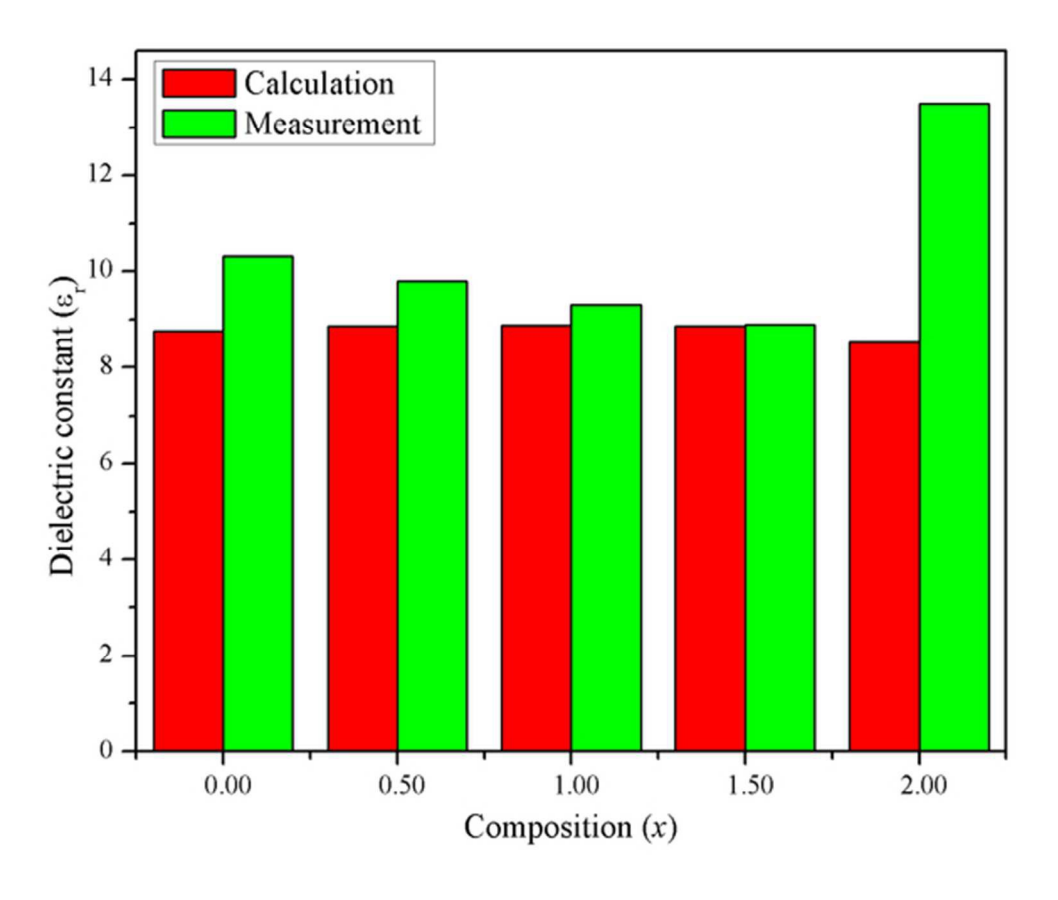


Figure 3 Dielectric constant plots of Cu(2-x)ZnxP2O7 ; x = 0.00 - 2.00. 50x42mm (300 x 300 DPI)

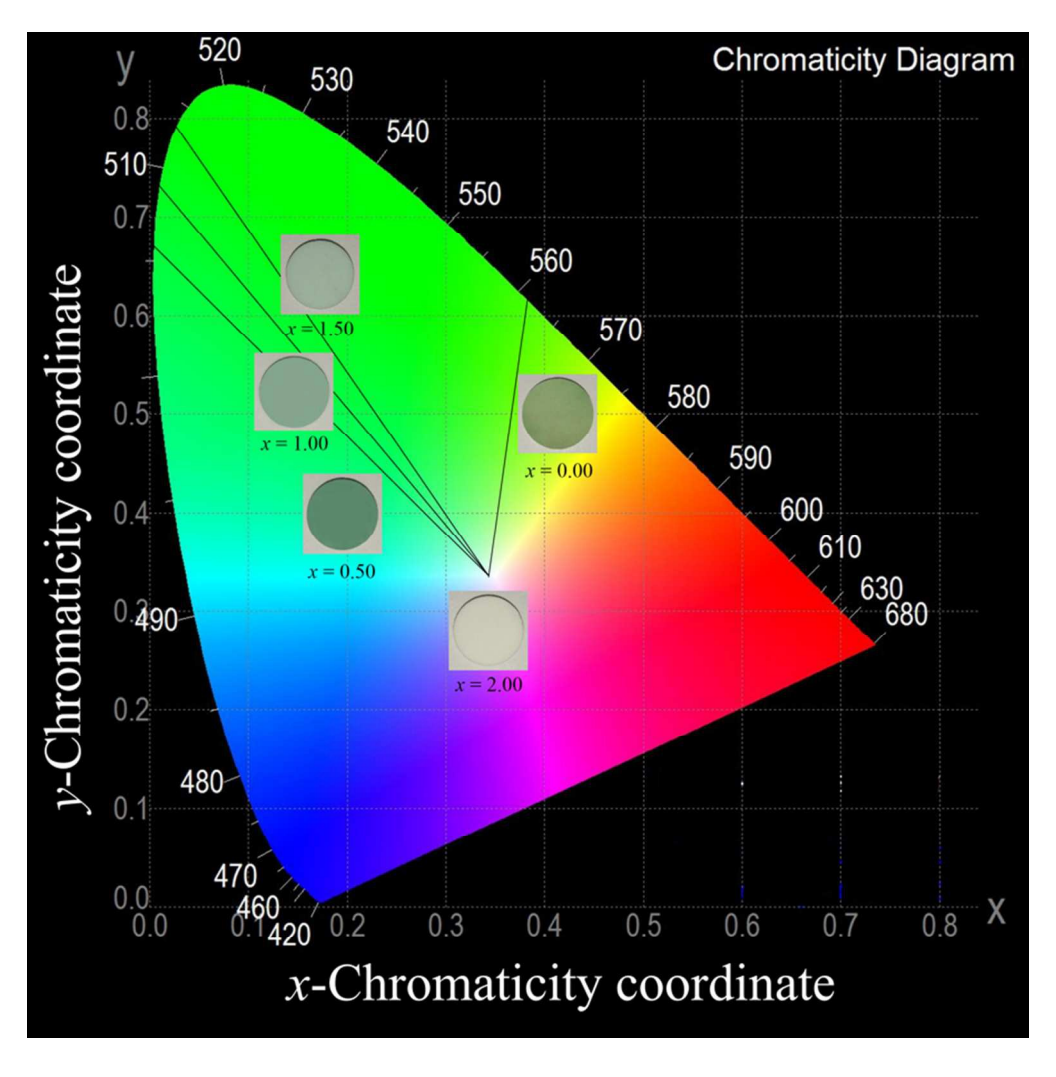


Figure 4 CIE chromatic coordinates of Cu(2-x)ZnxP2O7 ; x = 0.00 - 2.00. 76x76mm (300 x 300 DPI)

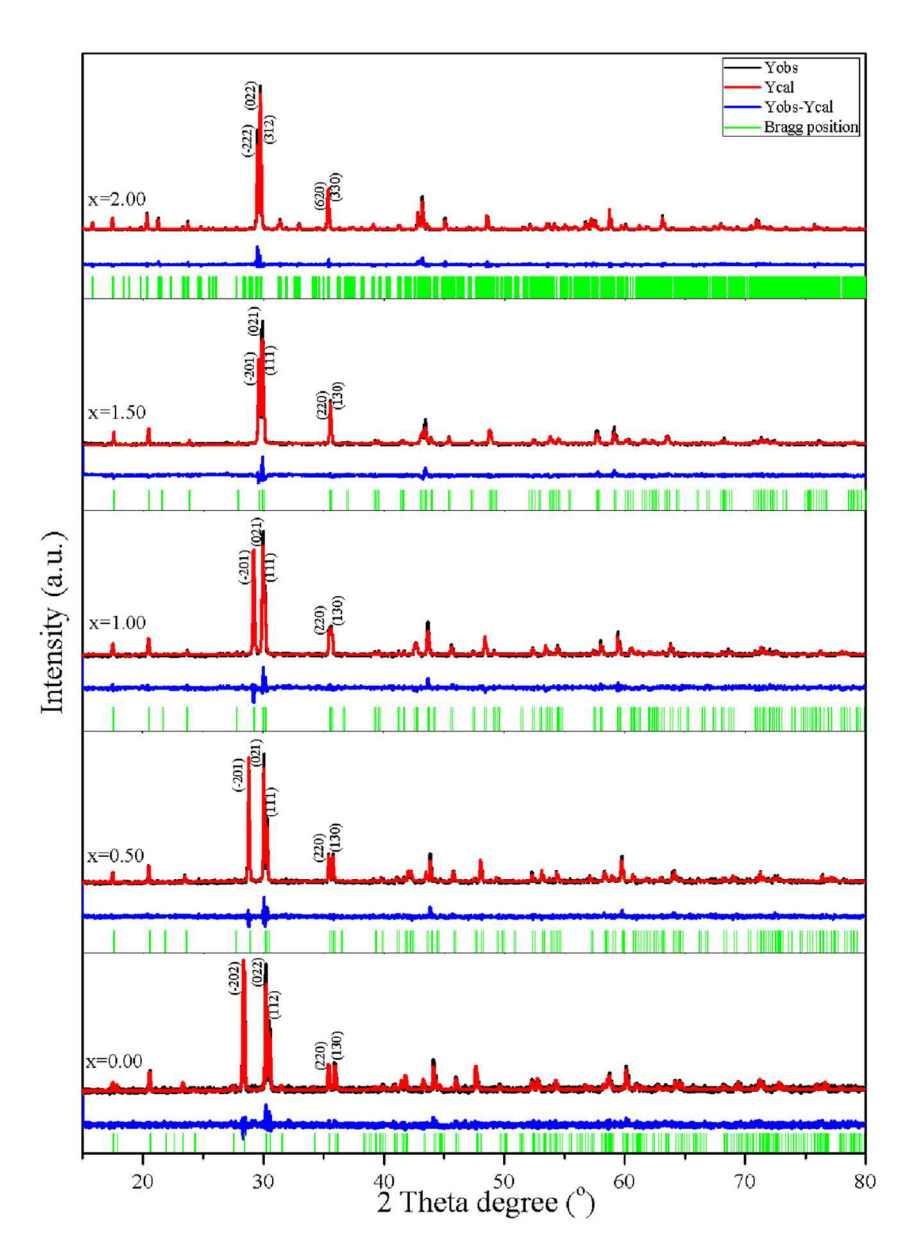


Figure 5 Rietveld refinement patterns of Cu(2-x)ZnxP2O7 ; x = 0.00 - 2.00. 99x140mm (300 x 300 DPI)

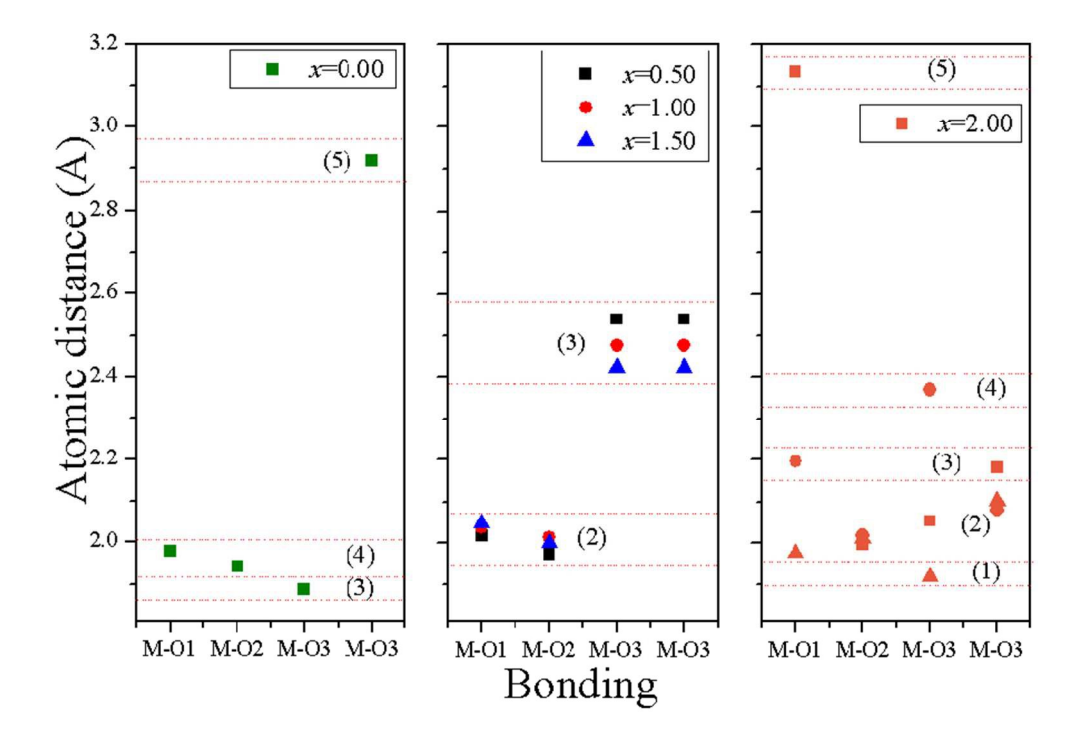


Figure 6. The approximate grouping of M-O bonding of Cu(2-x)ZnxP2O7 ; x = 0.00 - 2.00. 76x52mm (300 x 300 DPI)

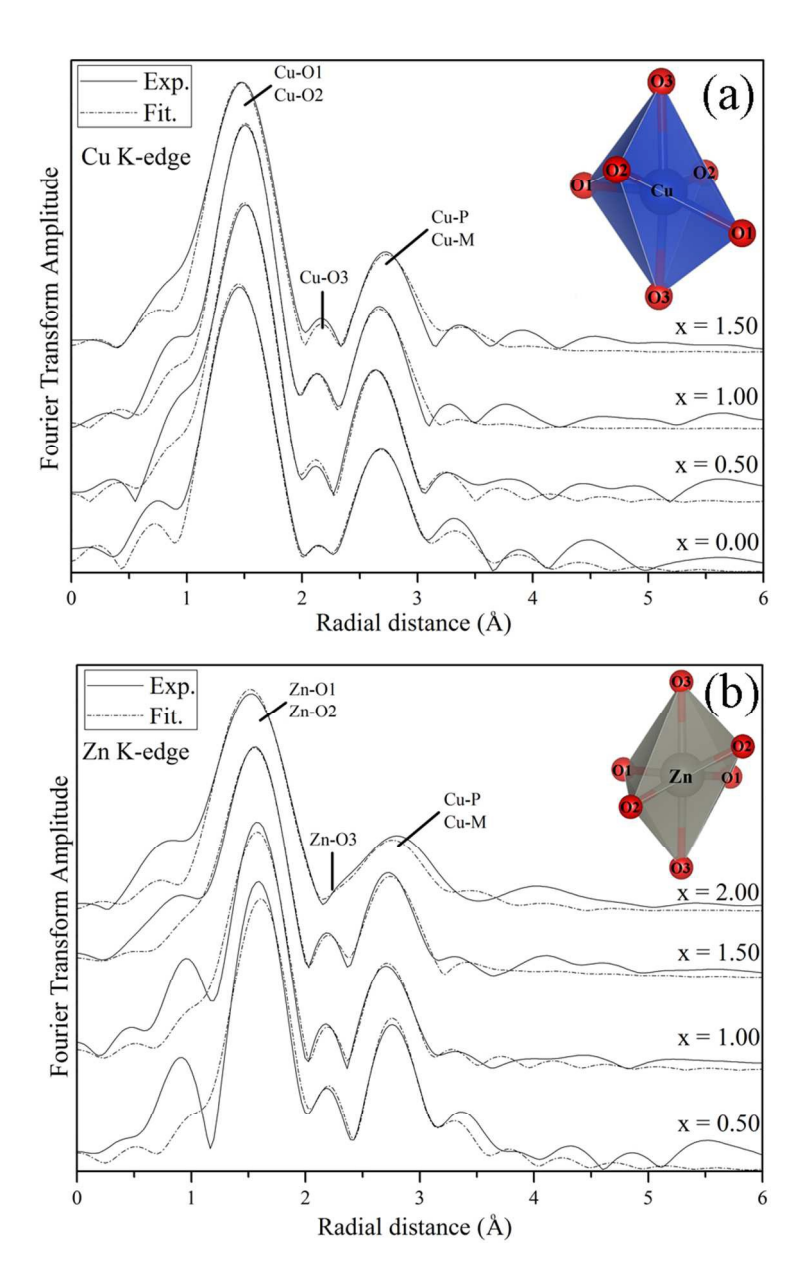


Figure 7 EXAFS fitting curves of Cu(2-x)ZnxP2O7 ; x = 0.00 - 2.00. 76x122mm (300 x 300 DPI)

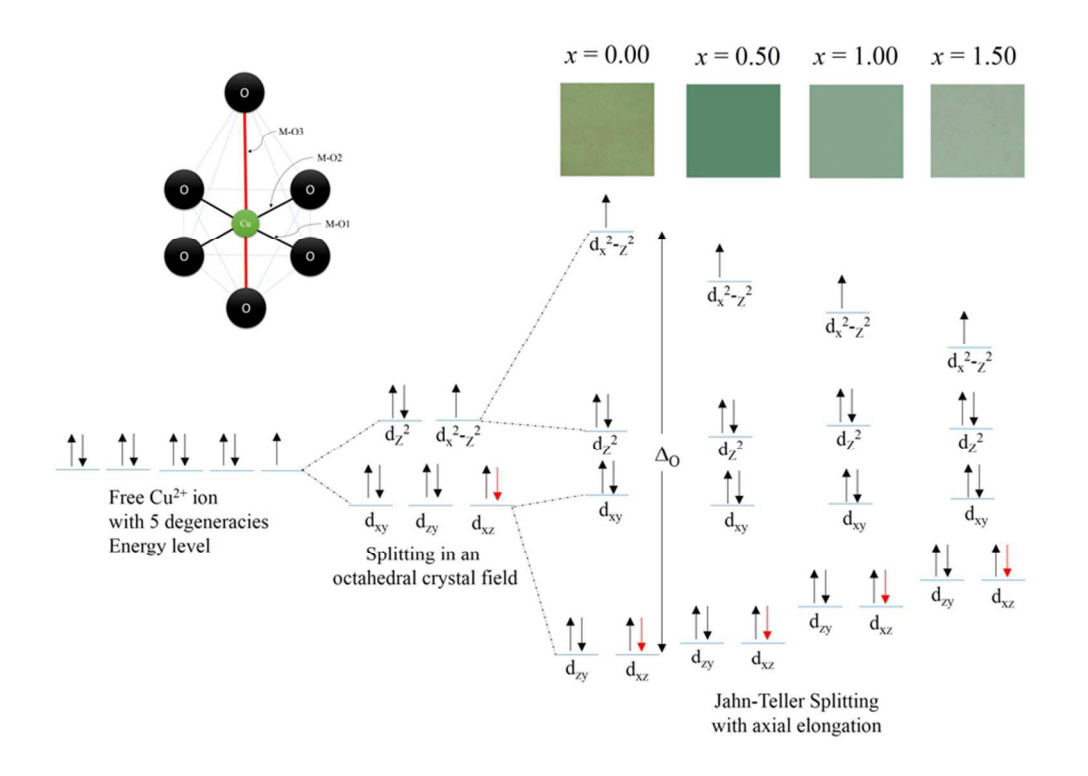


Figure 8 Summary of crystal field splitting in Cu(2-x)ZnxP2O7 ; x = 0.00 - 1.50. 76x55mm (300 x 300 DPI)